JOM, Vol. 75, No. 10, 2023
https://doi.org/10.1007/s11837-023-06053-5

Solid-State Additive Manufacturing of AA6060 Employing Friction Screw Extrusion Additive Manufacturing

S.S. REZAEINEJAD,[1,2] D.H. STRIK,[1,3] R.M. VISSER,[1,4] T.C. BOR ,[1,5] M. LUCKABAUER,[1,6] and R. AKKERMAN[1,7]

1.—Chair of Production Technology, Faculty of Engineering Technology, University of Twente, Drienerlolaan 5, 7522 NB Enschede, The Netherlands. 2.—e-mail: s.rezaei@utwente.nl. 3.—e-mail: d.h.strik@student.utwente.nl. 4.—e-mail: r.m.visser@utwente.nl. 5.—e-mail: t.c.bor@utwente.nl. 6.—e-mail: m.luckabauer@utwente.nl. 7.—e-mail: r.akkerman@utwente.nl

Solid-state additive manufacturing constitutes a worthwhile alternative for many precipitation-based aluminium alloys that cannot be processed through fusion-based approaches due to metallurgical problems. In this work, the newly developed solid-state friction screw extrusion additive manufacturing (FSEAM) approach has been employed to study the processability of AA6060 T6 as a function of the printing velocity. Various wall-like builds were fabricated at printing velocities of 100 mm/min to 250 mm/min by deposition of 50 layers of 1 mm thickness, 14 mm width, and 150 mm length. No major defects were observed in cross section, and the microstructure showed equiaxed grains with an average size of 2–4 μm for all builds. Promising mechanical properties were obtained for all tensile test specimens extracted in the deposition direction of the layers. For specimens extracted in the build direction, only the builds fabricated with sufficiently high normal force to ensure proper bonding between successively deposited layers showed similar results to the deposition direction. The relatively high temperatures obtained during fabrication led to the dissolution of strengthening precipitates for the 150–250 mm/min samples as indicated by serrated yielding effects. Post-manufacturing heat treatment of these samples was successful, partially restoring the feedstock hardness.

INTRODUCTION

Additive manufacturing (AM) techniques have gained increasing attention in recent years as a viable solution for the fabrication of intricate designs with different materials. However, fusion-based AM approaches are known to cause several problems during the melting and re-solidification of aluminium alloys, including porosity, hot cracking, high residual stresses, and evaporation of alloying elements.[1,2] In fusion-based additive manufacturing processes, the microstructure of the fabricated products often exhibits a preferred orientation of the grains, which can be attributed to the directional nature of the heat dissipation during the solidification of the liquid phase, usually leading to unwanted anisotropic properties of the final product.[3]

Solid-state AM approaches have attracted a significant amount of interest recently, owing to their ability to overcome many of the limitations associated with traditional fusion-based AM techniques.[4,5] In this work, the emphasis is on the freeform, direct AM approach that utilizes friction and severe plastic deformation (SPD) to soften, transport, deposit, and bond the feedstock on top of a substrate or previous layer below the onset of melting. Several of these approaches that build up or repair parts layer by layer, based on virgin or recycled materials, have been developed successfully, albeit typically with a relatively large width per layer exceeding 20 mm.[4–16] The builds are characterized by a fine microstructure with an average grain size of < 10 μm and by the absence

(Received April 27, 2023; accepted July 25, 2023; published online August 17, 2023)

of preferred grain orientation and fusion-based AM defects associated with melting and solidification. However, discernible reductions in strength and hardness values are typically observed when employing solid-state AM techniques on precipitation-based aluminium alloys, including those classified under the 2xxx, 6xxx, and 7xxx series.[1,12,16–20]

Friction Screw Extrusion Additive Manufacturing

This research study investigated the novel in-house developed solid-state additive manufacturing technique, friction screw extrusion additive manufacturing (FSEAM), based on the principles of friction stir welding (FSW).[21,22] FSEAM employs a screw-like rotating tool to generate heat through friction and SPD of the rod-shaped feedstock material. The tool transports the softened material toward the substrate/previous layer and deposits it in a sequential layer-by-layer fashion to fabricate the intended product. A schematic outline of the FSEAM setup used in this study is shown in Fig. 1, where Ω is the rotational speed of the tool, v_t is the velocity of the table/substrate, V_f is the volumetric supply rate of the feedstock, t is the vertical position of the exit opening, defining the layer thickness, and W is the width of the deposited layer.

The tool gap, depicted in Fig. 1b, is established by the vertical distance between the housing and the screw and can be customized before conducting experiments. The flow characteristics of the material, temperature, and pressure build-up during printing are all influenced by the tool gap. The precision of the deposited layers can be improved through the utilization of additional support edges, which act as a die located at the lower section of the housing. These support edges effectively avoid flash formation during the process and enhance the controllability over the width of the builds. The width of the deposited layer is denoted by W, while W_d represents the width of the die.

Feed Ratio

The volumetric supply rate of the feedstock V_f is in balance with the deposition rate of the material according to the principle of mass conservation. The required amount directly follows from the layer width, layer thickness, and print velocity through:

$$V_f = W \cdot t \cdot v_t$$

The feed ratio f is defined as the ratio of volumetric feeding supplied per unit of time to the volume of material required per unit of time based on a layer width equal to the distance between the support edges, W_d:

$$f = \frac{V_f}{W_d \cdot t \cdot v_t} = \frac{W}{W_d}$$

The feed ratio constitutes an important parameter in the FSEAM manufacturing process as learned from preliminary investigations.[22] Supplying just the right amount of material per unit of time to fabricate a build with layer thickness equal to the distance between the support edges, i.e., $W = W_d$ with $f = 1$, led to insufficient bonding between successively deposited layers yielding poor mechanical properties. Overfeeding, where f is greater than one, is effective in reducing manufacturing defects and achieving adequate intermixing between consecutive layers generating better mechanical performance.

Microstructure Development During and After FSEAM

The FSEAM process generates high temperatures and strain rates that can result in significant microstructural changes of the feedstock material while being transported and deposited. The dynamic nature of the process triggers multiple metallurgical mechanisms, including strain hardening, recovery, and recrystallization, which occur

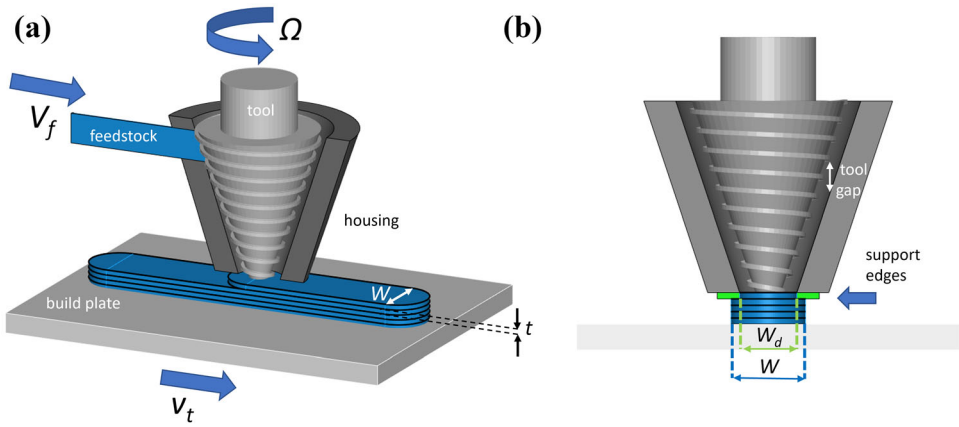

Fig. 1. Schematic outlines of (a) the FSEAM setup, (b) the tool gap, which is the vertical distance between the housing wall and the screw, and the additional support edges for FSEAM, which increase the precision of printing.

almost simultaneously and often lead to a notable reduction in grain size.[9,23,24] Although a smaller grain size is often associated with an increase in strength, the mechanical properties of medium and high-strength aluminium alloys are dominated by the amount, size, type, and distribution of precipitates. Growth and/or dissolution of precipitates and nucleation of clusters and/or new precipitates are additional mechanisms that play a significant role in the development of the mechanical properties in the as-fabricated state.[18,24] It is critical to monitor, evaluate, understand, and control these mechanisms during the transportation and deposition stages of the fabrication process to attain the desired microstructure, mechanical properties, and part performance.[25,26] Post-manufacturing heat treatment cycles can be included, for example, to modify the as-built microstructure and improve the mechanical properties.[27–30]

This study aims to analyse the impact of the FSEAM printing velocity on the macrostructure, microstructure, and mechanical properties of rectangular builds fabricated from AA6060 T6, which is used as a typical example of a medium-strength precipitation hardenable aluminium alloy. The study includes the effect of post-processing heat treatments on the mechanical properties of the manufactured builds.

MATERIALS AND METHODS

Materials and FSEAM Process

In this series of experiments, rectangular wall-shaped AA6060 builds were manufactured through FSEAM on top of AA2024 T351 substrate plates employing rod-shaped feedstock with a diameter of 8 mm and lengths up to 45 mm. The chemical composition (in wt.%) of the AA6060 T6 feedstock, used in this study, as determined by energy dispersive spectroscopy (EDS) measurement, is: Mg 0.5%, Si 0.4%, Fe 0.4%, Mn 0.1%, Cu 0.1%, Zn 0.1%, Ti $<$ 0.1%, Cr $<$ 0.1%.

The FSEAM process was successfully employed using a modified planer machine equipped with an in-house developed printing system consisting of a vertically oriented 13-kW electric motor driving a threaded tool placed in the stationary housing of the printhead. A dedicated nozzle with a Ø 10.5-mm opening was placed underneath the printhead. The feed material was supplied through a hydraulic cylinder attached to the side of the printhead.

The tool rotational speed and the tool gap were fixed during the experiments to 400 rpm and 3.2 mm, respectively. Four builds were manufactured through FSEAM, employing a printing/table velocity of 100 mm/min, 150 mm/min, 200 mm/min, and 250 mm/min. Each build consisted of 50 sequentially deposited layers with a uniform thickness of 1 mm and length of 150 mm. The feed ratio employed in each experiment was set to approximately 1.3, implying that an increase in printing velocity was met with a corresponding increase in the feeding rate, thereby preserving a constant feed ratio. Consequently, the width of the manufactured builds was expected to be around 14 mm, representing a 30% increase compared to the distance between the support edges of the die.

The temperature was measured through K-type thermocouples positioned at various locations in the setup and substrate. One thermocouple was placed relatively close to the nozzle opening of the printhead to approximately determine the feedstock material temperature during deposition. Additionally, the normal force, exerted on the substrate during deposition, was measured using three load cells placed equally around the circumference of the motor frame. A more comprehensive explanation of the setup and printing process has been presented recently.[22]

Microstructure and Mechanical Evaluations

The fabricated builds were sectioned into two pieces where one piece was employed for microstructure characterization, while the other was used for mechanical analysis.

Standard metallographic methods were used for surface preparation of the cross-sections. Grinding was carried out up to 4000 grit paper to eliminate surface irregularities, followed by diamond polishing with suspensions of 3 μm, 1 μm, and colloidal silica, to obtain a deformation-free surface suitable for microstructural evaluations. Some cross-sections were etched prior to microscopy using a solution of 10 g NaOH in 90 ml distilled water for 60–120 s to enhance the visibility and contrast of microstructural features.

The first analysis of the prepared cross sections was carried out through light microscopy (LM) employing a digital optical Keyence VHX 7000 microscope. The stitching function was employed to obtain a complete overview of the builds and their layers. Subsequently, scanning electron microscopy (SEM) using a Thermo Fisher Phenom XL and a JEOL JSM 7200f with EDS and electron backscatter diffraction (EBSD) detectors were utilized for further analysis to comprehensively characterize the microstructure. A back-scattered electron (BSE) detector was used for image acquisition to provide a comprehensive overview of different phases within the microstructure. Selected samples were embedded in conductive epoxy to improve image quality and prevent charging issues during EBSD imaging.

Vickers microhardness (HV) measurements were done on the cross-sectional plane along the height of the fabricated builds employing a 1-mm distance between subsequent indents. A 'Leco LM 100 AT' hardness tester was employed for this purpose, utilizing a force of 300 gf and a dwell time of 15 s.

Tensile test specimens were extracted from the horizontal (deposition direction) and vertical (build direction) orientations using electrical discharge

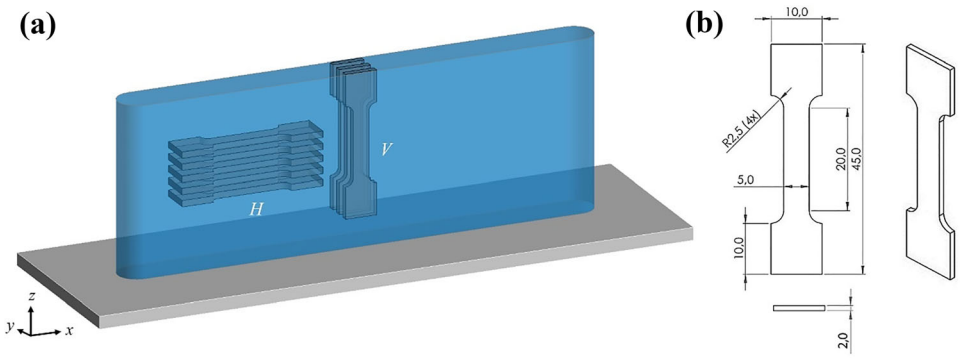

Fig. 2. (a) Approximate extraction locations of the horizontal (*H*) and vertical (*V*) tensile test specimens. Build length and height were about 150 mm and 54 mm, respectively. (b) Schematic drawing with dimensions of the non-standard tensile test specimens.

machining (EDM), assuring minimal mechanical stress and deformation. The approximate extraction locations of the tensile specimens are depicted in Fig. 2a. The dimensions of the non-standard tensile specimens were maintained at an overall length of 45 mm, thickness of 2 mm, and fillet radius of 2.5 mm, while the gage length and width were 20 mm and 5 mm, respectively. A schematic drawing of the tensile specimen is given in Fig. 2b.

Tensile tests were done using a Zwick Z100 mechanical tester with a load cell capacity of 100 kN. The specimens were sprayed and coated with a black–white speckle pattern paint on one side a day before testing to facilitate displacement measurements through the ARAMIS digital image correlation system. The system was equipped with a Titanar B camera and utilized the ARAMIS professional 2020 software.

The fracture surfaces of the tensile specimens were examined using SEM to discern the type of fracture and ascertain the potential influence of defects arising during the fabrication process of the builds.

For conducting the post-process heat treatment of the samples, cross-sectional pieces from the entire height of each build were put in a preheated furnace at 170°C for durations of 3 h and 20 h. The temperatures of the furnace and samples were carefully monitored throughout the experiments with a precision of ± 2°C employing K-type thermocouples. A dedicated thermocouple was positioned inside an aluminium block that held the samples to achieve accurate temperature monitoring. Microhardness measurements were conducted along the height of the heat-treated samples employing the microhardness device and procedures described above. The post-manufacturing heat treatments were carried out about 6 months after fabrication of the builds.

RESULTS AND DISCUSSION

Feed Ratio, Nozzle Temperature, and Normal Force

Results of the average nozzle temperature (T_{nozzle}), average normal force (F_{n}), and feed ratio (f_{exp}) as a function of the printing velocity (v_{t}) are shown in Fig. 3. The average nozzle temperature exhibited an upward trend with increasing printing velocity from 100 mm/min to 250 mm/min and a similar rising trend was observed for the average normal force, as also supported by the dashed trend lines that act as a guide to the eye. Apparently, the deposition of larger amounts of feedstock material per unit of time led to higher forces and more heat generation. The respective values for the experiments performed at 150 mm/min deviated from the trend lines, which was related to the use of an accidentally higher value of the feed ratio.

The intended feed ratio for all samples was f = 1.3, and the measured values for 100 mm/min, 200 mm/min, and 250 mm/min builds were found to be 1.31, 1.33, and 1.39, respectively. However, the feed ratio for the 150 mm/min sample was around 1.6, causing the average nozzle temperature and exerted normal force to exceed the expected levels based on the trend lines.

Build Appearance

A macroscopic image of the manufactured AA6060 build on top of an AA2024 substrate with a print velocity of 200 mm/min is depicted in Fig. 4a. The build has an approximate length of 150 mm in the x direction and a width of around 14 mm in the y direction, which corresponds to a feed ratio of 1.3 used in the experiments. The build consists of 50 layers, each with a thickness of 1 mm, deposited on top of each other in the z direction using a back-and-forth movement of the printhead. At the two endpoints of the builds, the width is larger compared to that of the mid-section as visible within both black dashed rectangles of Fig. 4a. This can be attributed to the relatively slow upward movement of the printhead before starting a new layer deposition.

Further details of the build from within the white dashed square of Fig. 4a are shown in Fig. 4b. The outer surface quality of the 200 mm/min sample is characterized by a relatively smooth surface with uniform edges as visible from the black dashed lines. The 150 mm/min and 250 mm/min sample

displayed a similar appearance, with smooth and consistent edges. In contrast, Fig. 4c depicts the build with 100 mm/min printing velocity, which displays a rougher appearance on the edges with a wavy shape, as indicated by undulating black dashed lines. The origin to the non-uniform shape of the build for the lower print velocity of 100 mm/min is under investigation.

Microstructure

For a more comprehensive analysis of the cross section, an overview of the bonded layers was acquired, using digital optical microscopy, as illustrated in Fig. 5a. This detailed examination was carried out in the upper region of the builds, as indicated by the black-dashed rectangle in Fig. 5b.

In all builds, a layer-by-layer structure was observed, and distinct flow patterns among individual layers were noted, which correspond to the material flow during the fabrication process. These flow patterns did not exhibit any apparent correlation with print velocity or feeding rates, as observed in different samples and various heights of the builds. It is hypothesized that the variation in grey colour among the layers could be attributed to slight differences in their microstructure, such as grain size or precipitate distribution, resulting in different reactions to the etchant. Further investigation is necessary to fully elucidate this phenomenon.

The excess value in the feed ratio for the 150 mm/min sample, as illustrated in Fig. 3, is reflected in the width of the build, which is noticeably larger than that of the other samples, as visible in Fig. 5a.

To examine the presence of interior defects like cracks and porosities that may arise during the manufacturing process, SEM analysis was carried out. The results indicated that at a lower print velocity of 100 mm/min, numerous cracks and unbonded areas were observed among the deposited layers, as shown by the white arrows in Fig. 5c. Limited interdiffusion and intermixing between the layers, likely caused by relatively low average normal forces and average nozzle temperatures (Fig. 3), could be responsible for the formation of these elongated crack-like defects. Conversely, for the sample with the high print velocity of 250 mm/

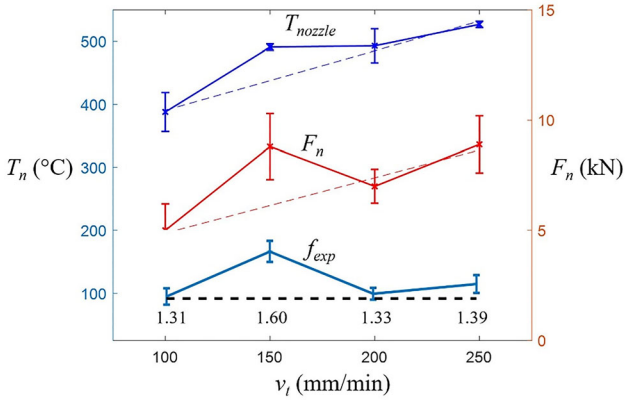

Fig. 3. Average nozzle temperature (T_{nozzle}), average normal force (F_n), and experimental feed ratio (f_{exp}) as a function of printing velocity (build velocity) during the FSEAM process. Dashed lines act as guides to the eye.

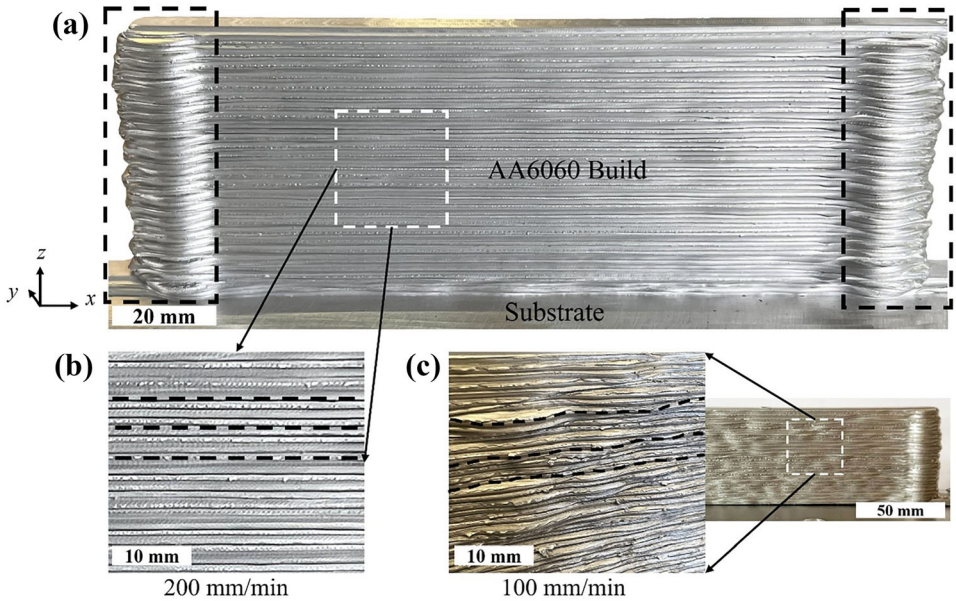

Fig. 4. (a) Macroscopic image of a printed AA6060 build through the FSEAM process on top of an AA2024 substrate using AA6060 T6 as the feedstock material. Black-dashed rectangles on both sides of the build indicate the larger width of the build due to the relatively slow vertical movement of the printhead in the *z* direction before starting a new layer deposition. (b) Further details of the surface quality of the 200 mm/min build, depicting a relatively smooth surface with fairly uniform edges. (c) Surface quality of the manufactured build with low printing velocity of 100 mm/min, exhibiting wavy edges and inhomogeneous appearance (Color figure online).

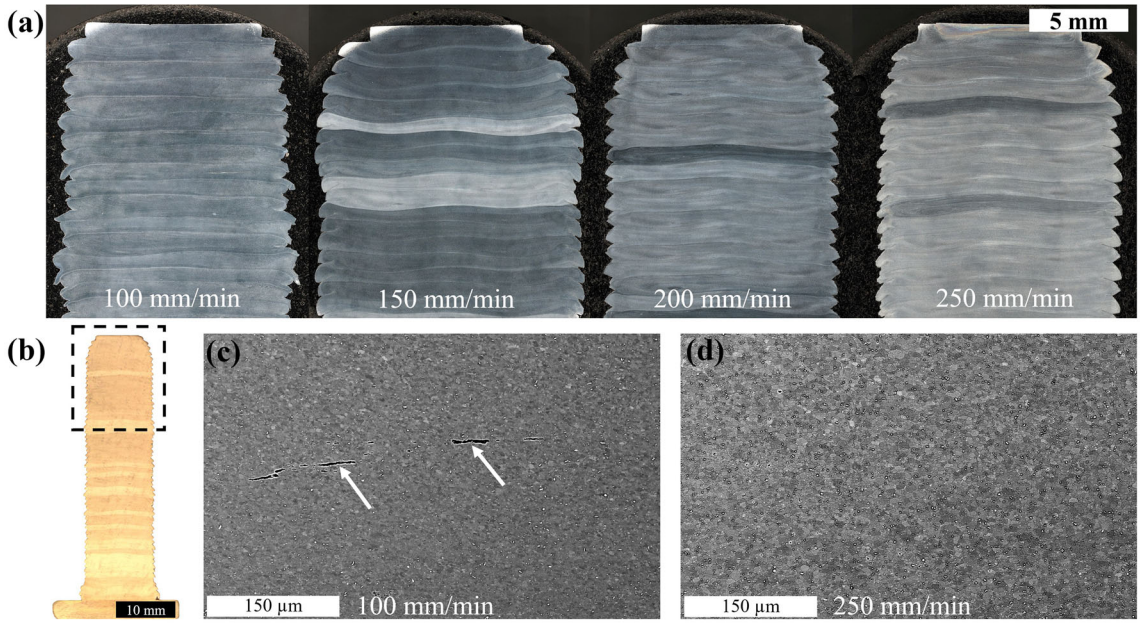

Fig. 5. (a) Overview image of the cross section of the manufactured builds with different printing velocities of 100 mm/min, 150 mm/min, 200 mm/min, and 250 mm/min. The scale bar is valid for all builds. (b) An overall cross section of a manufactured build with a black-dashed rectangle which indicates the area of the more-detailed investigations shown in (a). (c) Manufacturing defects that are frequently observed in the low printing velocity of 100 mm/min as a result of low bonding quality between subsequent layers, indicated by white arrows. (d) No major defects and good bonding condition between deposited layers in the printing velocity of 250 mm/min (Color figure online).

min, no major defects or unbonded regions were observed within the deposited layers upon SEM investigation. The improved interlayer mixing and diffusion, likely facilitated by higher average normal forces and average nozzle temperatures, according to Fig. 3, resulted in a more homogeneous and defect-free build, as demonstrated in Fig. 5d. Therefore, adequate temperature and normal force settings during the printing process are crucial factors in mitigating the occurrence of cracks and defects in fabrication of builds.

The above microstructural analysis was conducted throughout the entire height of the current builds, revealing no major differences in grain size. However, it has been reported that microstructural inhomogeneity can occur throughout the height of the builds because of the influence of deposition process variables such as temperature and pressure.[31,32] This means that the microstructural properties of previously deposited layers can be affected by the heat from the layers deposited at later stages of the manufacturing process.

To obtain a more in-depth understanding of the microstructure, EBSD measurements were conducted on the upper one third part of the builds, as indicated by the dashed box in Fig. 5b. The EBSD results revealed a well-refined equiaxed grain microstructure for all manufactured samples (Fig. 6a–d). The equivalent circle diameter (ECD) values of the grains were determined by analyzing the EBSD data with a scanned area of approximately 4500 μm^2. The average grain sizes of the fabricated builds, obtained from four different spots in the upper one third of each build, are included in the figure (see $< D >$) and varied between 2 μm and 4 μm for different printing velocities between 100 mm/min to 250 mm/min. Moreover, the microstructural evaluation conducted over the height of the samples revealed no significant change in grain size and particle/dispersoid distribution for each build. Hence, a very homogeneous appearance of the microstructure was observed throughout the height and width of each sample.

The variation in the average grain size among the additively manufactured builds can be explained by the microstructural phenomena of dynamic recrystallization (DRX), recovery, and grain growth during the FSEAM process.[24]

Recrystallization is a process of nucleation and growth of new grains from sufficiently deformed grains to reduce internal energy. Dynamic recrystallization (DRX) is a type of recrystallization that occurs during deformation at high temperatures and high strain rates, likely to be occurring during FSEAM. The phenomenon is responsible for the fine grains in all builds. Recovery is a process in which dislocations align and are partially annihilated, reducing the internal energy of the material which can occur simultaneously with DRX.[9,20]

Grain growth, on the other hand, is the increase in grain size due to prolonged exposure to high temperatures. In FSEAM, grain growth can occur because of the relatively high temperatures of the process, which promote diffusion of atoms and lead

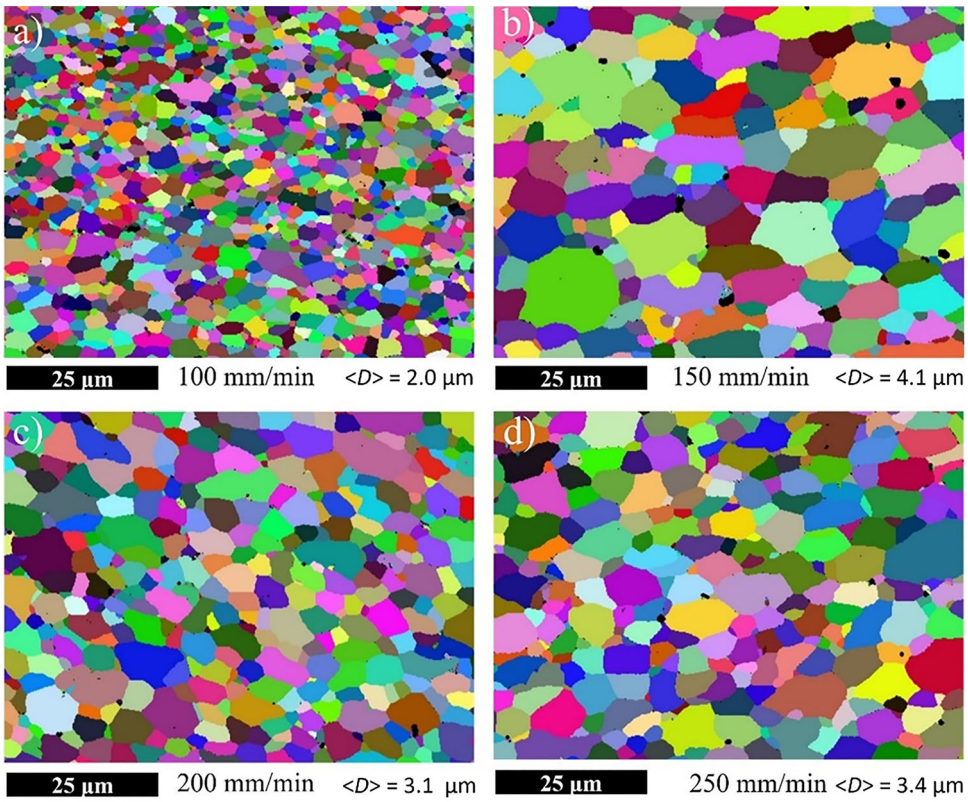

Fig. 6. (a)–(d) EBDS results of the fabricated builds with different printing velocities from 100 mm/min to 250 mm/min. Equivalent circle diameter values of the grains are indicated for each image, $< D >$.

to coarsening of grains. Figures 3 and 6 indicate that the lower average nozzle temperature of the 100 mm/min build led to stronger nucleation of new grains providing a smaller overall grain size compared to the other fabricated builds. In addition to the nozzle temperature, the amount of the deposited material affects the time required to dissipate heat. The sample printed at 150 mm/min had a greater amount of deposited material due to the higher feed ratio and thus retained heat for a longer duration, possibly resulting in facilitated grain growth.

Mechanical Characterization

Tensile Tests

To evaluate the mechanical properties of the fabricated builds, including yield strength, tensile strength, and ductility, tensile tests were conducted on each of them. Three vertical samples along the build direction and five horizontal samples along the translational direction were extracted from specific regions in each build, as shown in Fig. 2a. The ARAMIS measurement system was employed in tensile testing to determine the average engineering strain over the gage section of the tensile test specimen leading to the engineering stress-strain curves as presented in Fig. 7. The black and blue lines in the image represent the horizontal (H) and vertical (V) samples, respectively.

The samples extracted in horizontal direction, i.e., along the deposition direction, typically exhibited ductile behaviour characterized by a large plastic region, distinct necking area, and significant elongation after yielding. A linear trend of increased tensile strength was observed from 100 mm/min to 250 mm/min, while the yield strength remained relatively constant across all printing velocities, and the elongation at fracture slightly reduced approximately from 30% to 25%.

On the other hand, Fig. 7 shows that the tensile test results of the samples extracted in vertical direction, i.e., in the build direction, follow the results of the horizontal test specimens quite well for the first stages of the tests. However, at later stages of the tests for the printing velocities of 100 mm/min and 200 mm/min, a sudden drop is observed indicating premature and unexpected failure. These failures could be attributed to the presence of interior crack-like manufacturing defects and/or unbonded interlayer regions, as explained in Section "Microstructure," and shown for the 100 mm/min build in Fig. 5c, that typically occurred at the interface between successive layers. Hence, the larger number of layers that are part of vertical samples compared to horizontal ones make the vertical samples with their larger number of interlayer regions more prone to premature failure.

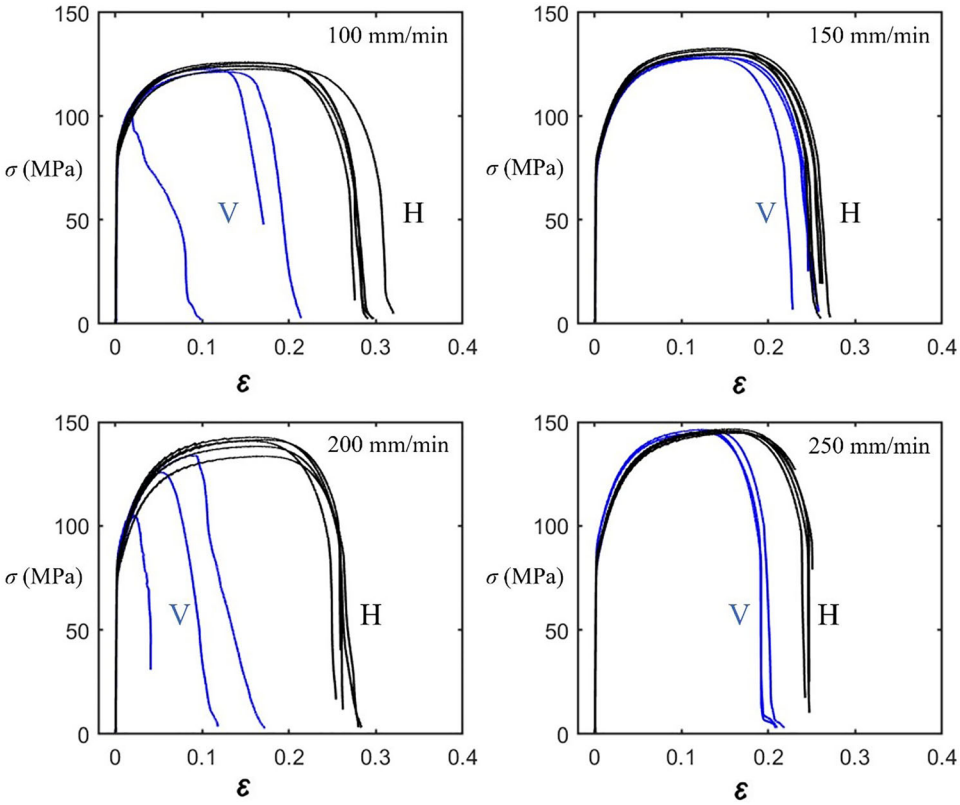

Fig. 7. Engineering stress–strain curves of the tensile experiments of the 100 mm/min to 250 mm/min builds conducted on the vertical (*V*) and horizontal (*H*) directions corresponding to build and deposition directions, respectively (Color figure online).

However, the results of the samples extracted from the 150 mm/min and 250 mm/min builds displayed a smaller difference in strength and ductility between horizontal and vertical samples, which could be ascribed to the relatively high normal forces observed during fabrication, see also Fig. 3, which limited the occurrence of interior defects.

The overview of all tensile test results is given in Fig. 8, where the mechanical properties evaluated for horizontal and vertical samples are represented by solid and dashed lines, respectively. The manufactured builds exhibited a tensile strength ranging from 120 MPa to 145 MPa as function of the printing velocity. These values are lower than the tensile strength of the AA6060 T6 feedstock, which is approximately 210 MPa. The yield strength of the fabricated samples experienced a decrease to a value of around 80 MPa, independent of the printing velocity, compared to 150 MPa for the feedstock. The elongation at fracture of the manufactured builds was in the range of 25–30%, which is larger than the corresponding value for the feedstock, which is about 10%.[33]

The results of the tensile tests, in combination with the normal forces applied during the process, suggest that a normal force of approximately 8–10 kN is necessary to ensure adequate bonding between layers, at least given the current design of the setup with a flat tool bottom. Further

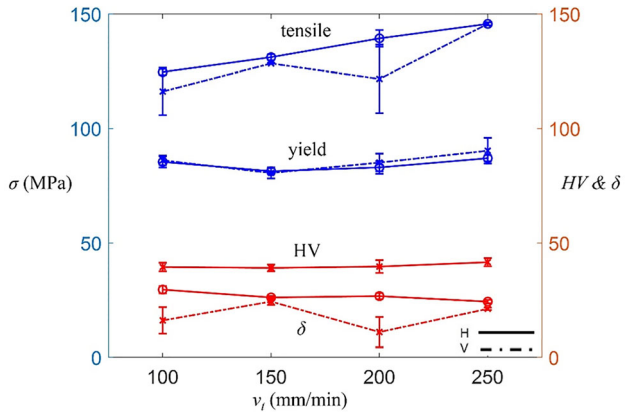

Fig. 8. Overview of the mechanical properties results of the manufactured builds, including tensile strength, yield strength, elongation at fracture (δ), and Vickers microhardness (HV), in two different directions, horizontal (solid lines) and vertical (dashed lines).

investigation and optimization of the printing parameters are expected to lead to improved quality of the vertical samples and equal mechanical properties in deposition and build direction.

Upon analysing the results of the tensile test presented in Fig. 9a, which shows one tensile result in the horizontal direction for each build, it was observed that three stress–strain curves possess

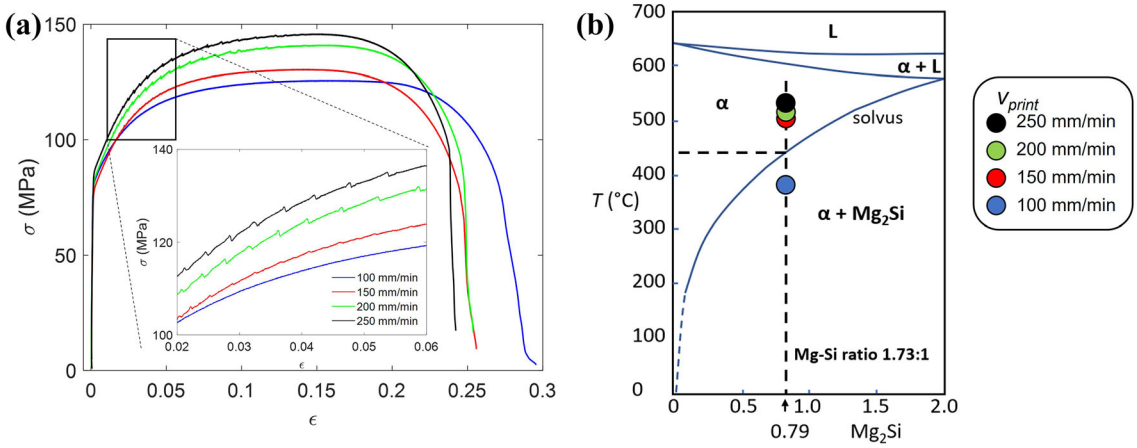

Fig. 9. (a) Serrated yielding effect in tensile samples of the AA6060 fabricated builds with different printing velocities from 100 mm/min to 250 mm/min. (b) Pseudo-binary phase diagram of Al-Mg_2Si and the correlation between the average nozzle temperature during the FSEAM process for all builds with printing velocities from 100 mm/min to 250 mm/min (Color figure online).

serrated appearance in the plastic region before necking. This phenomenon has been reported to occur in various aluminium alloys, including the 6xxx series, during tensile tests, and is often compared to the Portevin–LeChatelier (PLC) effect found in carbon steels.[34–36]

One proposed model to explain this phenomenon is the interaction between dislocations and solute atoms/atomic clusters. The solute atoms diffuse towards the area around the dislocations, effectively pinning them by reducing their stress fields. As the tensile force increases, the dislocations must surpass this atmosphere to move and cause further deformation. The release of pinned dislocations leads to small drops in the stress-strain curve, which ultimately results in the observed serrations. Consequently, this phenomenon can only be detected if a substantial amount of free solute atoms is available in the aluminium matrix.[34,37] In fact, the magnitude of the serrated yielding effect is influenced by the number of solute atoms and a higher concentration of solute atoms leads to a stronger serrated yielding.[34]

During the FSEAM process, high strain rates and elevated temperatures cause growth and/or dissolution of precipitates in the microstructure. In the latter case, an increase in the concentration of solute atoms is expected, which can trigger the appearance of serrated yielding in the stress-strain curves. The analysis of the tensile results for the 100 mm/min sample did not show any signs of serrated yielding. In Fig. 9b, the pseudo-binary phase diagram of Al-Mg_2Si is shown. The measured composition of the AA6060 alloy used for the experiments is indicated by the vertical dashed line. Above 450°C, the material is a single-phase α solid solution. However, the average nozzle temperature for the 100 mm/min sample, according to Fig. 3, is about 384°C, represented by a circular blue dot in Fig. 9b, which was insufficient to dissolve the precipitates in the microstructure, thereby preventing the formation of free solutes and the emergence of serrated yielding.

Conversely, in the case of the other samples (150 mm/min, 200 mm/min, and 250 mm/min), the average nozzle temperature during manufacturing was > 450°C, as shown in Fig. 3 and depicted in Fig. 9b by the circular red, green, and black dots, respectively, indicating that the temperature was sufficient for precipitate dissolution. However, the magnitude of the serrations varies across these samples, which possibly relates to the temperature level of the process to dissolve the precipitates. The average nozzle temperature of the 250 mm/min sample is relatively higher than the 150 mm/min sample, resulting in a faster dissolution of precipitates and causing a higher concentration of solute atoms, which in turn leads to a stronger intensity of serrated yielding.[34] Evidently, the cooling rates experienced by the deposited layers after deposition also depend on the maximum temperature achieved, but apparently, the cooling rates were high enough for a significant number of solute atoms to remain in solution to explain the occurrence of the serrated yielding effect.

Fractography

Fractography was employed in both horizontal and vertical directions for printing velocities of 100 mm/min and 250 mm/min to assess the fracture behaviour of the tested tensile samples. The results of the fractographic analysis conducted in the vertical direction for both printing velocities using LM and SEM are presented in Fig. 10a–f. The vertical direction was selected as it represents the most critical direction for the tested samples.

The macroscopic image of the fractured tensile sample of the 100 mm/min build in vertical direction showed little deformation and a small necking area, as shown in Fig. 10a. The vertical samples printed at 100 mm/min suffered premature failure caused

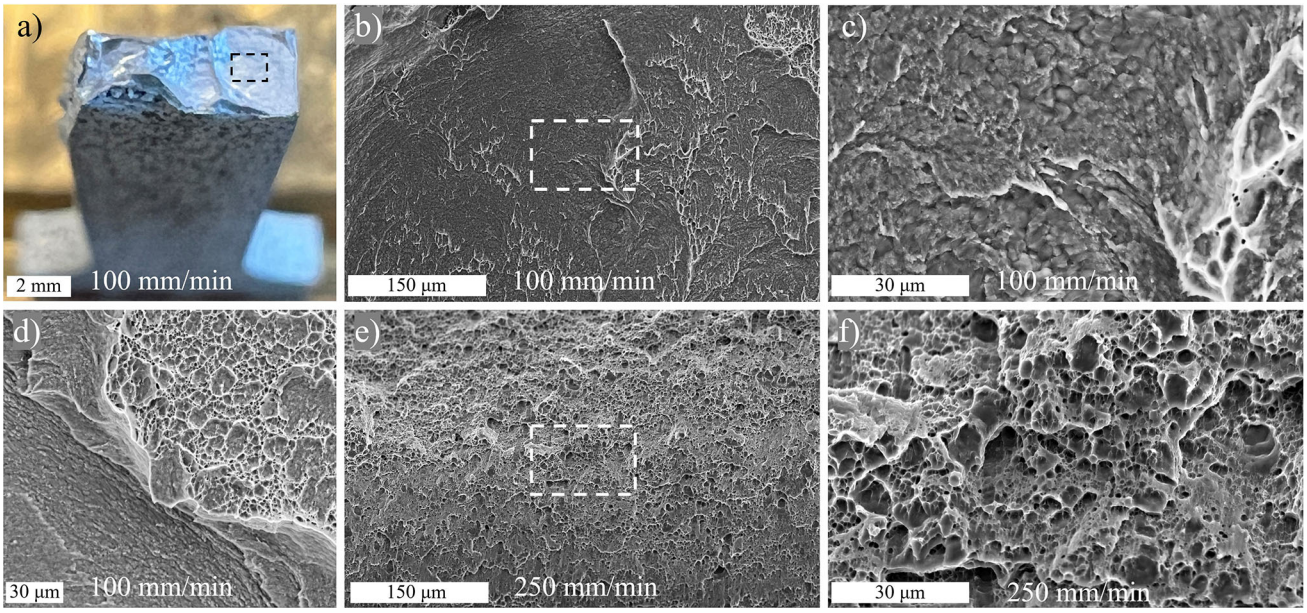

Fig. 10. (a) Macroscopic image of fractured tensile sample of the 100 mm/min build in vertical direction, showing small deformation and necking area. (b) Fracture surface of 100 mm/min sample performed on the rectangular black dashed area in (a), representing shear-like fracture. (c) More detail of the area indicated by white dashed rectangle in (b). (d) Two different modes of fracture, known as dimple fracture and shear-like fracture, next to each other in the 100 mm/min sample. (e) Fracture surface of 250 mm/min sample. (f) More detail of the area indicated by white dashed rectangle in (e), showing a dimple-rich fracture surface (Color figure online).

by interior elongated crack-like defects, as noted in Section "Tensile Tests." Therefore, the fracture surface exhibited a shear-like pattern combined with shallow dimples, indicating a small amount of ductility, shown in Fig. 10b and in more detail in Fig. 10c. Also, in Fig. 10d, two different types of fracture, dimple fracture and shear-like fracture, related to the 100 mm/min sample are visible.

Conversely, the 250 mm/min sample showed a well-developed dimple-rich fracture surface with a deep cup-and-cone pattern and distributed large and small dimples, which is a common pattern in aluminium alloys exhibiting adequate elongation in the plastic region.[20,38] Dimple fractures occur because of micro-void coalescence, where the material deforms significantly before fracturing.[38] The elongation in the plastic region is associated with the ability of the material to absorb energy before fracture. Figure 10e presents the fracture surface of the 250 mm/min sample, while Fig. 10f reveals more detail of the area indicated by the white dashed rectangle in Fig. 10e.

These findings provide important insight into the fracture behaviour of the tested samples and will be useful in optimizing the printing parameters to minimize the occurrence of defects and enhance the mechanical performance of the printed components.

Hardness and Heat Treatment

Vickers microhardness measurements were conducted throughout the height of each build in the midplane of the cross-sectional area. The average hardness for each sample was around 40 HV with a marginal increase in the hardness as the printing velocity increased from 100 mm/min to 250 mm/min; see Fig. 8. The hardness was strongly reduced compared to the value of 80 HV of the AA6060 T6 feedstock.

The hardness profiles through the height of AA6060 fabricated builds with printing velocities of 100 mm/min and 250 mm/min, representing the lowest and highest speeds, respectively, are illustrated in Fig. 11. The results are shown in three different conditions: as-printed (AP), aged for 3 h at 170°C (3 h), and aged for 20 h at 170°C (20 h). The dashed lines in Fig. 11a and b serve as a visual aid for referencing the value of the feedstock.

Upon analysing the hardness values for the 100 mm/min and 250 mm/min samples in the as-printed condition, it can be inferred that the hardness remains nearly constant through the height of both builds with small variations. However, a slight increase in the hardness value was noticed in the uppermost layers of the 250 mm/min sample, as signified by the blue arrow in Fig. 11b.

After the application of two different heat treatment cycles to both specimens, a negligible rise in the hardness value (approximately 5%) across the complete height of the 100 mm/min sample was identified; see Fig. 11a. Conversely, the 250 mm/min sample demonstrated a substantial increase (around 25%) in hardness throughout the entire build. Remarkably, the top six to seven layers exhibited an increase of even 60% compared to the as-printed state, indicated by the black arrow in Fig. 11b. Interestingly, there was no significant

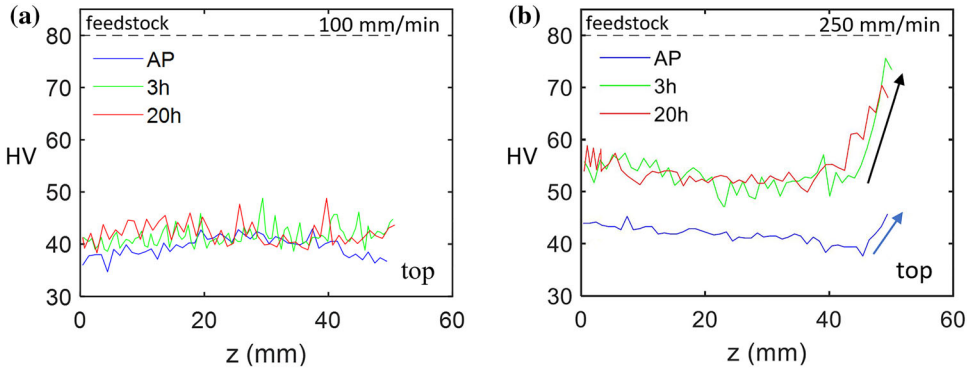

Fig. 11. Hardness profiles through the height of AA6060 builds with varying printing velocities: (a) 100 mm/min and (b) 250 mm/min, in three conditions: as-printed (AP), aged at 170°C for 3 h (3 h), and 20 h (20 h) (Color figure online).

difference in the hardness values observed between both heat treatment durations for both samples.

The observed hardness increase of the 250 mm/min sample confirms the presence of available free solute after build fabrication that forms additional strengthening precipitates during the post-process heat treatment. The results are in line with the observations of serrated yielding in Fig. 9 for this sample. The stronger hardness increase in the top layers of the sample can be attributed to the variation in overall heat input in the different layers at varying heights during fabrication. Specifically, the topmost layers receive less heat input as they are not subject to further layers being printed above them. Consequently, they experience shorter 'ageing' times as compared to the lower layers, leaving more solute atoms in supersaturation in the as-printed state. This difference in thermal history results in differences in mechanical properties and creates mechanical inhomogeneity within the build.[31,32] The absence of a hardness increase upon post-process heat treatment for the 100 mm/min sample is attributable to the average nozzle temperature that remained below 450°C during the FSEAM process, failing to dissolve the precipitates in the microstructure. Consequently, the post-process heat treatment did not influence the hardness value. These findings provide evidence of the effectiveness of the post-processing ageing heat treatment as a means to restore the hardness value, and possibly other mechanical properties, in printed components that reach a sufficiently high temperature during the process to dissolve precipitates and subsequently are cooled rapidly enough to maintain a certain degree of super saturation.[27,38]

Thermal Process Description for FSEAM

Figure 12 presents a thermal process description for understanding the in situ heat treatment during the FSEAM process, which can be linked to the typical T6 heat treatment cycle involving homogenization, quenching, and artificial ageing, thereby providing the maximum strength and hardness. The description interconnects the FSEAM process with the pseudo-binary phase diagram of the AA6060 alloy and heat treatment cycles occurring during and after the process. As shown in Fig. 12, the supplied material experiences high temperatures in the processing area, and homogenization occurs in the microstructure corresponding to the α solid solution region of the pseudo-binary phase diagram (this step is depicted by yellow areas). The deposition process follows, causing quenching from the high temperature α solid solution area to the two-phase region $\alpha + Mg_2Si$, as represented by the blue areas in Fig. 12. Ageing may occur in the $\alpha + Mg_2Si$ region utilizing the heat of the subsequently deposited layers, which should ideally take place in the temperature range indicated by the green area in Fig. 12.

After performing FSEAM with different printing velocities, as discussed in this study, it has been found that the ageing temperature is presumably too high for achieving an optimal size, type, and distribution of the strengthening precipitates to optimally enhance the build's mechanical properties as schematically depicted by the grey areas. In other words, an in-process ageing heat treatment at an appropriate temperature and time could create optimal precipitates, regarding their size, type, and distribution, which will lead to enhanced hardness and strength in as-built state or after post-process ageing.

This process description provides greater clarity on the influence of individual steps and engaging parameters during the FSEAM process on the microstructural and mechanical properties of the manufactured product. Such clarity, in turn, enhances the controllability of the process, enabling greater control over the microstructure of the build product. Further investigations are required to regulate the process parameters to achieve the appropriate time and temperature requirements.

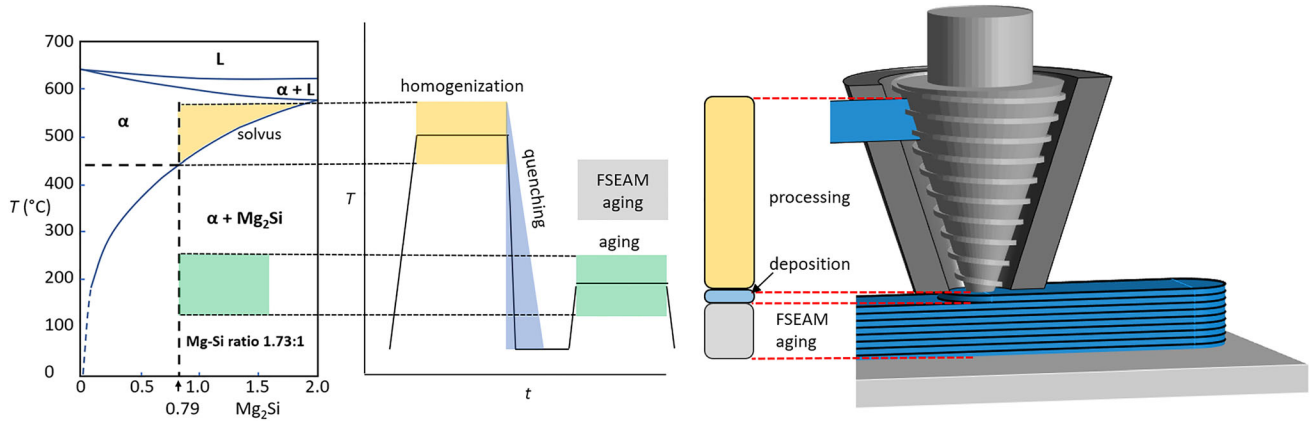

Fig. 12. Schematic model of in-situ heat treatment cycle happening during the FSEAM process for AA6060. Areas with similar colours represent the simultaneous phenomena. Current build conditions presumably involve too high ageing temperatures causing a non-optimal hardness after fabrication (Color figure online).

CONCLUSION

In this research work, the newly developed FSEAM process as a solid-state additive manufacturing approach was employed to fabricate builds of AA6060 T6, and the effect of different printing velocities from 100 mm/min to 250 mm/min on the processability, microstructure and mechanical properties was studied.

The results revealed that solid builds free from macroscopic defects could be fabricated through the consecutive deposition of layers by applying enough normal force at elevated temperature.

The microstructure analysis exhibited fine equiaxed grains with average dimensions of 2–4 μm without detectable crystallographic texture.

Tensile test results performed in both the deposition direction (horizontal) and the build direction (vertical) displayed tensile strength values increasing from 120 MPa to 145 MPa, and elongation at fracture decreasing from 30% to 25%, as a function of printing velocity. Best performance was obtained for the horizontal tensile samples, while the results of the vertical samples were strongly dependent on the process temperature and exerted normal force. The 250 mm/min samples in the build direction exhibited promising results presumably because of sufficient intermixing between subsequent layers and the absence of non-bonded regions.

The stress-strain curves showed the presence of serrated yielding for the builds manufactured at high enough temperatures to reach the single phase region according to the pseudo-binary Al-(Mg, Si) phase diagram at the AA6060 composition.

Hardness values of the manufactured builds were affected by the thermo-mechanical nature of the FSEAM process. Accordingly, a hardness reduction from 80 HV in T6 condition to 40 HV in as-built condition was observed. A post-manufacturing heat treatment partially improved the hardness when the initial process temperature was high enough to dissolve the precipitates and increase the amount of solute atoms/atomic clusters in the microstructure, especially when the process induced reheating time was relatively short.

A shear-like fracture pattern instead of ductile, dimple-rich fracture surface was observed for the samples with small, crack-like deposition defects confirming preliminary failure from the tensile tests for samples in the vertical build direction.

The FSEAM process requires further optimization to improve the mechanical properties in the as-printed condition and to allow for an optimized post-process heat treatment.

ACKNOWLEDGEMENTS

This work has been supported by Dutch Research Council (OCENW.XS21.1.078).

CONFLICT OF INTEREST

The authors assert that they have no identifiable financial conflicts of interest or personal associations that could be perceived as potentially influencing the findings presented in this manuscript.

OPEN ACCESS

REFERENCES

1. R.S. Mishra, R.S. Haridas, and P. Agrawal, *Sci. Technol. Weld. Join.* 27, 141 https://doi.org/10.1080/13621718.2022.2027663 (2022).
2. F. Khodabakhshi and A.P. Gerlich, *J. Manuf. Process.* 36, 77 https://doi.org/10.1016/j.jmapro.2018.09.030 (2018).
3. R.S. Mishra and S. Thapliyal, *Mater. Des.* 204, 109640 https://doi.org/10.1016/j.matdes.2021.109640 (2021).
4. N. Tuncer and A. Bose, *JOM* 72, 3090 https://doi.org/10.1007/s11837-020-04260-y (2020).
5. S.C. Altıparmak, V.A. Yardley, Z. Shi, and J. Lin, *Int. J. Lightweight Mater. Manuf.* 4, 246 https://doi.org/10.1016/j.ijlmm.2020.12.004 (2021).
6. S. Liu, T.C. Bor, A.A. Van der Stelt, H.J.M. Geijselaers, C. Kwakernaak, A.M. Kooijman, J.M.C. Mol, R. Akkerman, and A.H. van den Boogaard, *J. Mater. Proces. Technol.* 229, 769 https://doi.org/10.1016/j.jmatprotec.2015.10.029 (2016).
7. J. Blindheim, Ø. Grong, U.R. Aakenes, T. Welo, and M. Steinert, *Procedia Manuf.* 26, 782 https://doi.org/10.1016/j.promfg.2018.07.092 (2018).
8. R.J. Griffiths, M.E.J. Perry, J.M. Sietins, Y. Zhu, N. Hardwick, C.D. Cox, H.A. Rauch, and H.Z. Yu, *J. Mater. Eng. Perform.* 28, 648 https://doi.org/10.1007/s11665-018-3649-3 (2019).
9. H.Z. Yu and R.S. Mishra, *Mater. Res. Lett.* 9, 71 https://doi.org/10.1080/21663831.2020.1847211 (2021).
10. H.A. Derazkola, F. Khodabakhshi, and A.P. Gerlich, *J. Mater. Res. Technol.* 9, 15273 https://doi.org/10.1016/j.jmrt.2020.10.105 (2020).
11. J.B. Jordon, P.G. Allison, B.J. Phillips, D.Z. Avery, R.P. Kinser, L.N. Brewer, C. Cox, and K. Doherty, *Mater. Des.* 193, 108850 https://doi.org/10.1016/j.matdes.2020.108850 (2020).
12. R. Xie, Y. Shi, H. Liu, and S. Chen, *Mater. Today Commun.* 29, 103005 https://doi.org/10.1016/j.mtcomm.2021.103005 (2021).
13. R.B. Gottwald, R.J. Griffiths, D.T. Petersen, M.E.J. Perry, and H.Z. Yu, *Acc. Mater. Res.* 2, 780 https://doi.org/10.1021/accountsmr.1c00098 (2021).
14. M. Soujon, Z. Kallien, A. Roos, B. Zeller-Plumhoff, and B. Klusemann, *Mater. Des.* 219, 110786 https://doi.org/10.1016/j.matdes.2022.110786 (2022).
15. H. Chen, X. Meng, J. Chen, Y. Xie, J. Wang, S. Sun, Y. Zhao, J. Li, L. Wan, and Y. Huang, *Addit. Manuf.* 70, 103557 https://doi.org/10.1016/j.addma.2023.103557 (2023).
16. F. Liu, P. Dong, A.S. Khan, Y. Zhang, R. Cheng, A. Taub, and Z. Ma, *J. Mater. Sci. Technol.* 139, 126 https://doi.org/10.1016/j.jmst.2022.08.017 (2023).
17. G. Wu, C. Liu, L. Sun, Q. Wang, B. Sun, B. Han, J.J. Kai, J. Luan, C.T. Liu, K. Cao, Y. Lu, L. Cheng, and J. Lu, *Nat. Commun.* 10, 5099 https://doi.org/10.1038/s41467-019-13087-4 (2019).
18. J.K. Yoder, R.J. Griffiths, and H.Z. Yu, *Mater. Des.* 198, 109288 https://doi.org/10.1016/j.matdes.2020.109288 (2021).
19. C. Zeng, H. Ghadimi, H. Ding, S. Nemati, A. Garbie, J. Raush, and S. Guo, *Materials (Basel).* https://doi.org/10.3390/ma15103676 (2022).
20. B.J. Phillips, C.J.T. Mason, S.C. Beck, D.Z. Avery, K.J. Doherty, P.G. Allison, and J.B. Jordon, *J. Mater. Process. Technol.* 295, 117169 https://doi.org/10.1016/j.jmatprotec.2021.117169 (2021).
21. T.C. Bor, D.H. Strik, S.S. Rezaeinejad, N.G.J. Helthuis, G.S. Vos, M. Luckabauer, and R. Akkerman, in *Friction Stir Welding and Processing XII*. ed. by Y. Hovanski, Y. Sato, P. Upadhyay, A.A. Naumov, and N. Kumar (Springer, Cham, 2023), pp. 27–38. https://doi.org/10.1007/978-3-031-22661-8_3.
22. T. Bor, Md. Leede, F. Deunk, J. Lind, W. Lievestro, H.-J. Smit, R. Ariës, V. Dolas, N. Helthuis, M. Luckabauer, and R. Akkerman, *Addit. Manuf.* 72, 103621 https://doi.org/10.1016/j.addma.2023.103621 (2023).
23. R. Sudhish and K.U. Bhat, *Mater. Today Commun.* 31, 103354 https://doi.org/10.1016/j.mtcomm.2022.103354 (2022).
24. M.E.J. Perry, H.A. Rauch, R.J. Griffiths, D. Garcia, J.M. Sietins, Y. Zhu, Y. Zhu, and H.Z. Yu, *Materialia* 18, 101159 https://doi.org/10.1016/j.mtla.2021.101159 (2021).
25. Z. Shen, M. Zhang, D. Li, X. Liu, S. Chen, W. Hou, Y. Ding, Z. Sun, Y. Su, W. Li, and Y. Tian, *Int. J. Adv. Manuf. Technol.* 125, 2733 https://doi.org/10.1007/s00170-023-10952-x (2023).
26. A. Mukhopadhyay and P. Saha, *J. Braz. Soc. Mech. Sci. Eng.* 44, 422 https://doi.org/10.1007/s40430-022-03729-y (2022).
27. B. Chaudhary, N.K. Jain, J. Murugesan, and D. Sathiaraj, *Mater. Today Commun.* 34, 105156 https://doi.org/10.1016/j.mtcomm.2022.105156 (2023).
28. A.S. Sundar, A. Kumar, and K.K. Mugada, *Mater. Lett.* 327, 133010 https://doi.org/10.1016/j.matlet.2022.133010 (2022).
29. S.H. Wang, C.H. Liu, J.H. Chen, X.L. Li, D.H. Zhu, and G.H. Tao, *Mater. Sci. Eng. A* 585, 233 https://doi.org/10.1016/j.msea.2013.07.061 (2013).
30. X.-W. Yu, J.-H. Chen, W.-Q. Ming, X.-B. Yang, T.-T. Zhao, R.-H. Shen, Y.-T. He, and C.-L. Wu, *Acta Metall. Sin. (Engl. Lett.)* 33, 1518 https://doi.org/10.1007/s40195-020-01082-4 (2020).
31. M.B. Williams, T.W. Robinson, C.J. Williamson, R.P. Kinser, N.A. Ashmore, P.G. Allison, and J.B. Jordon, *Metals*. https://doi.org/10.3390/met11111739 (2021).
32. O.G. Rivera, P.G. Allison, L.N. Brewer, O.L. Rodriguez, J.B. Jordon, T. Liu, W.R. Whittington, R.L. Martens, Z. McClelland, C.J.T. Mason, L. Garcia, J.Q. Su, and N. Hardwick, *Mater. Sci. Eng. A* 724, 547 https://doi.org/10.1016/j.msea.2018.03.088 (2018).
33. Nedal Aluminium B.V., EN-AW 6060 (AlMgSi) Alloy Data Sheet (Nedal Aluminium, 2018), https://www.nedal.com/wp-content/uploads/2019/07/NEDAL_Datasheet-6060.pdf. Accessed 30 Apr 2023.
34. W. Wen and J.G. Morris, *Mater. Sci. Eng. A* 354, 279 https://doi.org/10.1016/S0921-5093(03)00017-0 (2003).
35. W. Wen and J.G. Morris, *Mater. Sci. Eng. A* 373, 204 https://doi.org/10.1016/j.msea.2004.01.041 (2004).
36. B. Gruber, I. Weißensteiner, T. Kremmer, F. Grabner, G. Falkinger, A. Schökel, F. Spieckermann, R. Schäublin, P.J. Uggowitzer, and S. Pogatscher, *Mater. Sci. Eng. A* 795, 139935 https://doi.org/10.1016/j.msea.2020.139935 (2020).
37. L. Rath, Z. Kallien, A. Roos, JFd. Santos, and B. Klusemann, *Int. J. Adv. Manuf. Technol.* 125, 2091 https://doi.org/10.1007/s00170-022-10685-3 (2023).
38. L. Yuan, X. Zeng, X. Zhao, Y. Xie, J. Gandra, and D. Guan, *Mater. Sci. Eng. A* 864, 144589 https://doi.org/10.1016/j.msea.2023.144589 (2023).